Microscale characterization of rupture nucleation unravels precursors to faulting in rocks

François Renard[1,2,] *, Benoît Cordonnier[1,3], Maya Kobchenko[1], Neelima Kandula[1], Jérôme Weiss[2], and Wenlu Zhu[4]

[1]Departments of Geosciences and Physics, PGP, University of Oslo, box 1048 Blindern, 0316, Oslo, Norway

[2]Univ. Grenoble Alpes, CNRS, ISTerre, 38000 Grenoble, France

[3]ESRF – The European Synchrotron, CS40220, Grenoble 38043, France

[4]Department of Geology, University of Maryland, College Park, MD 20742, USA

* Correspondence to: francois.renard@geo.uio.no

Keywords: fault, rupture, damage, X-ray microtomography

Abstract

Precursory signals, manifestations of microscale damage that precedes dynamic faulting, are key to earthquake forecasting and risk mitigation. Detections of precursors have primarily relied on measurements performed using sensors installed at some distance away from the rupture area in

both field and laboratory experiments. Direct observations of continuous microscale damage accumulated during fault nucleation and propagation are scarce. Using an X-ray transparent triaxial deformation apparatus, we show the first quantitative high resolution three-dimensional (3D) information about damage evolution of rocks undergoing brittle failure. The dynamic microtomography images documented a spectrum of damage characteristics and different fault growth patterns. The interplay between various deformation mechanisms can result in either a positive, negative, or constant net volume change. Consequently, changes in rock density and acoustic wave velocities before faulting are expected to vary in different tectonics settings, hence making failure forecasting intrinsically dependent on rock type at depth.

1. Introduction

In the Earth's crust, faulting and fault rupture release a significant part of the elastic strain energy that accumulates due to tectonic loading, gravitational relaxation, and industrial activities such as underground fluid injection and extraction. The existence of precursory signals (Jones and Molnar, 1979; Ellsworth and Beroza, 1995; Bouchon et al., 2011; Kato et al., 2016) to such ruptures is a very old problem and it may provide the key to failure forecasting (de Arcangelis et al., 2016). Variations of geophysical or geochemical signals have been reported before major earthquakes (Ellsworth and Beroza, 1995; Bouchon et al., 2011), volcanic eruptions (Kato et al., 2015), and cliff collapses (Amitrano et al., 2005), however they are not ubiquitous and vary with geological settings (Bouchon et al., 2013). The occurrence of small seismic events weeks to hours before a major earthquake (Kato et al., 2016) has been interpreted in terms of small seismic or aseismic slips along the fault plane (Guglielmi et al., 2015). The distribution of microearthquake magnitudes in the foreshock area may also vary before an earthquake or a volcanic eruption with

a change in Gutenberg-Richter frequency-magnitude b-value (Sugan et al., 2014) interpreted as related to high stress concentration, dilatancy in the fault zone, and propagation of fractures. Geochemical proxies, such as the concentration of radon gas in soils (Hauksson, 1981), and sulfate and chloride anions in spring waters (Tsunogai and Wakita, 1995; Toutain et al., 1997) have been observed to increase days before an earthquake (Wakita, 1996). These events are thought to be caused by the opening of cracks preceding dynamic faulting that provide paths for the migration of these chemical species towards the surface. Even when such precursory signals have been detected, their amplitude varies spatially, their existence is not ubiquitous, and the physical processes that enable migration from depth to the surface cannot be observed directly. Here, we present experimental evidence of the nucleation and propagation of such precursory deformations at the microscale. We show how small variations of porosity self-organize prior to a catastrophic failure and how their dynamics varies between different rock types, allowing the identification of different paths to fault initiation.

Small deformations preceding a large rupture are detected in both field and laboratory studies. Field observations are performed using seismometer and GPS networks located at the surface of the Earth, several kilometers away from the earthquakes hypocenters. In laboratory, acoustic emissions of damage prior to failure has been recorded and analyzed (Lockner et al., 1991; Zang et al., 2000; Schubnel et al., 2007; Benson et al., 2008). However, a limitation of acoustic emission damage characterization comes from the low spatial resolution of source location, particularly in heterogeneous rocks. To date, few direct in-situ 3D images of such damage processes have been obtained at the scale of whole rock samples, and most have been obtained under shallow depth stress conditions (Lenoir et al., 2007; Hall, 2013; Zhu et al., 2016).

Using a state-of-the-art triaxial deformation apparatus (Renard et al., 2016) that is transparent to the high flux of X-rays produced by a synchrotron, we studied the microscale damage evolution in rocks as they were driven towards brittle failure by increasing the differential stress at constant pressure confining pressure. Because the adsorption of X-rays depends on the local density of the solid, the evolution of microscale damage in the forms of microfracturing and pore-collapse during deformation can be monitored in 3D in centimeter-size core samples with a spatial resolution of 6.5 micrometers, as the differential stress is increased under stress conditions at depths of several kilometers (Figure 1). The time-resolved 3D images document the interplay of a variety of deformation mechanisms and the corresponding microscale damage leading to faulting (Figure 2, Video S4 to S6). The style and amount of damage determine the variations of the bulk density and acoustic wave velocities of rocks as they approach faulting.

2. Material and Methods

Several cylindrical cores, 4 or 5 mm in diameter and 10 mm in length, were taken from larger blocks of Carrara marble, Adamswiller sandstone, Fontainebleau sandstone, quartz-rich monzonite, Bentheim sandstone, and Anstrude limestone, with initial porosities in the range 0.5-19% and grain sizes in the range 0.1-0.7 mm. These rocks were chosen because they cover rock types from compact crystalline to porous siliciclastic and carbonate rocks. Some of them have very homogeneous composition, e.g., almost pure calcium carbonate for the marble and limestone and almost pure quartz for the Fontainebleau sandstone. Most of them contain strong heterogeneities (i.e., polymineralic grains) and pores, one to two orders of magnitude smaller than the dimensions of the core samples.

Experiments were conducted using an X-ray transparent triaxial deformation apparatus which enables the confining pressure (0 - 100 MPa), differential stress (0 – 200 MPa), temperature (25 –

88 250 °C), and fluid pressure (1 - 100 MPa) to be controlled independently (Figure S1). The
89 deformation apparatus, HADES (Renard et al., 2016), is installed on an X-ray microtomography
90 rotation stage at beamline ID19 at the European Synchrotron Radiation Facility in Grenoble,
91 France. During each deformation experiment, the apparatus is rotated over 180° and 1800 X-ray
92 radiographs can be acquired with a voxel size of 6.5 micrometers and estimated beam energy of
93 90 keV.

94 The experimental conditions are given in Table 1. All samples were deformed following the same
95 procedure. First, a sample is compacted hydrostatically by increasing the axial stress and
96 confining pressure equally. Once the hydrostatic confinement reaches a preset value (P_c, see
97 Table 1), the first X-ray tomography scan was performed to obtain the initial state of the sample
98 before deformation starts. Then, while keeping the confining pressure constant, the axial stress
99 was increased by increments of 5 MPa at the beginning, and then by 2 or 1 MPa when the
100 differential stress exceeds 50% of the shear strength of the sample. After each stress increment, a
101 3D X-ray microtomography scan was acquired at constant stress, until the sample failed by shear
102 faulting. Each step of stress increase lasted for 1 to 2 minutes, and each tomography scan lasted
103 for 3 minutes. The experiments were performed at room temperature and under nominally dry
104 conditions. The reconstruction of the 3D volumes from the radiographs was performed at
105 beamline ID19 at the ESRF, using both X-ray adsorption and phase contrast imaging (Mirone et
106 al., 2014). Time resolved 3D volumes of the whole sample were acquired for each deforming
107 rock.

108 The stress-strain curve was plotted for each sample by measuring, on the 3D microtomography
109 images, the shortening of the rock core with increasing differential stress (Figures 1b, S2). The
110 3D volumes were analyzed using the software Avizo™ to extract both the solid phase (grains)

and the voids (porosity, microfractures) from the X-ray images obtained during each experiment. Because the gray levels of the pore space and of the solid grains were well separated (Figure 3), only a simple procedure was needed to extract the void space. First, the 3D volumes were denoised based on a non-local averaging of all pixels in the image (non-local means filtering technique described in Buades et al. (2005). Then, a gray level threshold was applied to separate the empty voids from the solid matrix. The same threshold was applied to all the 3D volumes of a given experiment and all individual voids were extracted. The processed data contained the position, volume, and surface area of each individual void (microfracture or pore). Consequently both changes in voids volume and surfaces area, as well as the creation of new voids can be determined after each stress increment. To test the effect of the choice of the threshold during the void segmentation procedure, several thresholds around the minimum of the histogram (a gray level of 7750 in Figure 3), were used. The relationship between the damage index (see section 3.2 below) and the distance to faulting varied only moderately if the segmentation threshold was varied slightly, as Figure 4 illustrates for the Bentheim sandstone.

This technique of high resolution in-situ imaging is novel and complement existing imaging techniques in rock physics such as imaging from acoustic emission locations and ultrasonic velocities. With an acquisition time close to one minute, X-ray microtomography is still not quite fast enough to capture the very quick coalescence of microfractures observed by Lockner et al. (1991). However, the dynamic imaging presented here allows understanding 3D porosity development, crack anisotropy and the role of heterogeneities in general at the scale of a whole sample.

3. Results

The failure mode of rocks changes from brittle faulting in the seismogenic Earth's crust to mainly ductile flow at larger depths, as pressure and temperature increase (Paterson and Wong, 2005). In the brittle faulting regime, laboratory experiments have demonstrated that the deformation behavior preceding shear failure can be characterized by three stages: i) a non-linear regime at low stress related to the closing of pre-existing cracks or pores, ii) a linear elastic regime at moderate stress, followed by iii) a non-linear regime above a yield point related where irreversible deformations at scales smaller than that of the sample size (i.e., microscale damage) play an important role. During this last phase, damage increases and precursors can be detected in the tomography data (Figure 1a). Then, the rock breaks at a failure threshold σ_f along a macroscopic fault that relaxes part of the remaining stress. This sequence of mechanical behaviors occurred for all the rocks deformed in this work (Figures 1b, S2).

3.1 Three modes of failure

Three modes of failure characterize the evolution of damage with increasing stress in the various rocks. In the first mode, observed in both the Fontainebleau sandstone (Figures 1b inset, 2a), a porous siliciclastic rock, and the quartz monzonite, a compact crystalline rock, microfractures opened initially at grain boundaries or within grains. These microfractures initially opened as mode I cracks, parallel to the main compressive stress. They aligned predominately along a well-defined plane with a mean angle of inclination at around 30° with respect to the direction of the maximum compressive stress, σ_1 (Figure 1). Linkage of these microfractures formed a finite size fault (Lockner et al., 1991; Zang et al., 2000). Near the fault tip, a high density of microfractures was observed within a small volume whose size is of the order of the grain size of the rock. This observation is consistent with the development of a finite-sized process zone (Bažant and Kazemi, 1990), also referred to as a damage zone or plastic zone. In the second mode of failure,

represented by the Carrara marble, a rock with almost no porosity and composed of nearly 100% calcite, microfractures initially appeared indiscriminately and pervasively throughout the rock. Multiple parallel shears develop and spread across the sample, and at a late stage conjugate shears developed. As the sample approached failure, the microfractures clustered along a localized shear band oriented at around 30° with respect to σ_1 that subsequently coalesced into a rupture plane (Figures 1a, 2b). The sample failed by symmetric bulging in the middle by shearing on both sets of shear planes. This is classical cataclastic failure, and is typical of such ductile rocks as marble. The main difference between the first two modes of failure is that for the first one the damage extends at the fault tip only (Video S4), whereas for the second modes microfractures nucleate pervasively in the volume before localization of a fault (Video S5). The third mode of failure was observed in highly porous rocks, including Anstrude limestone (Figures 1b inset, 2c, Video S6), and Adamswiller and Bentheim sandstones. At the onset of yield in these rocks, the microscale damage is controlled by the interplay between two competing processes: on the one hand microfractures cause dilatancy, on the other hand the closure of preexisting pores leads to compaction. As a result, a net volume decrease was observed before failure in both the Anstrude limestone (Figure 5) and Bentheim sandstone, whereas no significant macroscopic density variation was measured for the Adamswiller sandstone (Figure S3). This is the typical behavior of high porosity rocks. At the field scale, shearing occurs by the formation of deformation bands, which are compaction features (Aydin and Johnson, 1978) rather than by dilatant cracks or faults. The deformation of such highly porous rocks in laboratory experiments differs as well (Mair et al., 2000).

3.2 Evolution of damage prior to failure

The three modes of failure presented above suggest that, for similar stress-strain relationships, the evolution of damage during fault nucleation and propagation can be markedly different even though the stress-strain relationships are similar. This can be quantified by defining a damage index $(\phi-\phi_i)/(1-\phi_i)$, where ϕ is the porosity of the sample at a given stress and ϕ_i is the initial porosity of the undeformed sample. This index is positive for dilation and negative for compaction. It measures the magnitude of the porosity variations compared to the initial porosity. It can be calculated directly from the 3D microtomography data from which the voids can be extracted by a segmentation procedure (Figures 3, 4). For some samples, the damage index increased as microfractures or a main fault nucleated and grew with increasing loading, for other samples it remained constant or even decreased when pore collapse occurred (Figures 5, S3). When σ_f, the stress at faulting, was approached (Figure 5), the damage index varied differently depending on the rock type. For Carrara marble, the acceleration of damage towards rupture followed a power-law singularity $\frac{\phi-\phi_i}{1-\phi_i} \sim \left(\frac{\sigma_f-\sigma}{\sigma_f}\right)^{-\nu}$ with $\nu \approx 2$ (Figure 6), in line with the proposition that rock brittle failure and earthquakes could be related to the establishment of long range correlations in the stress field, and considered as critical phenomena (Jaumé and Lynn, 1999). For the other rocks, the damage index increased almost linearly, remained constant, or decreased towards rupture (Figures 6, S3).

3.3 Estimation of strain energy dissipation in low porosity rocks

We calculate the strain energy budget for experiments in which rocks with very low porosity (Carrara marble and quartz-monzonite) were loaded until failure. We consider E, the initial Young's modulus, and ε_0 the "initial" strain in the absence of initial crack closure (Figure 7a).

We approximate the mechanical work per unit volume Ω_1 done to the sample by the axial force up to the stress at failure σ_f by

$$\Omega_1 = \int_0^{\varepsilon_f} \sigma d\varepsilon,$$

where σ is the differential stress, ε is the axial strain, and ε_f the axial strain at failure. Note that this represents a lower limit of the work, as the diameter of the sample would change during loading and the radial strain would increase Ω_1 under these confining pressure conditions. To estimate the part of the work that is dissipated irreversibly during loading, two end-member hypotheses can be proposed for the unloading scenario.

In the first hypothesis, the elastic damage case, at σ_f the rock is considered to be a purely elastic but damaged solid, with a Young's modulus lower than the intact rock. As a consequence, upon unloading the strain would come back either to $\varepsilon=0$ or $\varepsilon=\varepsilon_0$ if we neglect the initial crack closure process (Figure 7b). These two options ($\varepsilon=0$ or $\varepsilon=\varepsilon_0$) are only marginally different. To obtain the work converted into damage or heat before failure, one should remove the reversible elastic work $\Omega_2 = \frac{1}{2}\sigma_f \varepsilon_f$, or $\Omega_2 = \frac{1}{2}\sigma_f(\varepsilon_f - \varepsilon_0)$, from Ω_1. The difference $(\Omega_1 - \Omega_2)$ corresponds to the irreversible strain energy into the sample from micro-damaging and other dissipation mechanisms.

In the second hypothesis, giving an upper limit on the amount of mechanical work dissipated during loading, we assume that the rock is a purely plastic material at the point of failure and that it acts as a linear elastic material when it is unloaded. Under these circumstances, one can consider an unloading path that would follow the initial Young's modulus E (Figure 7c), i.e. the material is undamaged in the elastic sense (no effect on the elastic properties) but has undergone

a purely plastic (irreversible) deformation $\varepsilon_p = \varepsilon_f - \frac{\sigma^f}{E}$. The associated recovered work $\Omega_3 = \frac{1}{2}\frac{\sigma_f^2}{E}$ is necessarily smaller than Ω_2, and so the dissipated energy $(\Omega_1 - \Omega_3)$ is larger. The reality for the dissipated strain energy prior to failure falls necessarily in between $(\Omega_1 - \Omega_3)$ (plastic hypothesis) and $(\Omega_1 - \Omega_2)$ (elastic damage hypothesis). These various energies for the Carrara marble and the quartz-monzonite, as well as the ratio between the surface energy due to the creation of microfractures and the damage strain energy are calculated in the Table 2.

Because each microfracture can be extracted in the 3D image, the surface area of each of them can be calculated. A cumulated created surface of SA=2000 m^2/m^3 is calculated for the Carrara marble at the onset of failure. Considering a specific surface energy of γ_0 = 50 J/m² for marble (Friedman et al., 1972), a cumulated surface energy per unit volume of ≈ 100000 J/m^3 is estimated. For the quartz monzonite, the created surface area is 520 m^2/m^3, the specific surface energy is taken similar to that of granite γ_0 = 50 J/m² (Friedman et al., 1972), and the surface energy per unit volume is close to 26000 J/m^3. These values are always below the net amount of mechanical work converted into other forms of energy, as expected. However, they also mean that a significant percentage of the total dissipated energy (~4 to 46 %) corresponds to surface energy in the form of surfaces of the microfractures. Note that the estimated created surface area is a lower limit, because fractures with very small aperture widths or diameters may not be detected with a resolution (voxel size) of 6.5 micrometers, and the diameters of microfractures may be underestimated because of their small aperture widths near their perimeters. The remaining fraction of the irreversible strain energy could be dissipated by damage at scales smaller than the resolution of the images, or by plastic strain, or by heat dissipation by frictional sliding along existing interfaces.

4. Discussion and conclusion

Classical brittle failure criteria, such as the Coulomb's theory of faulting, ignore precursory phenomena, hence implicitly consider failure as a first order transition, in strong disagreement with the observations reported above. As shown in our experiments, the stress change during the microfracture nucleation to rupture transition (between the yield stress and the rupture stress) can be insignificant (e.g., Figure 1b), and thus the precursory signals associated with microscale damage should be taken into account in failure prediction. In the field and laboratory experiments, acoustic recording of elastic waves produced by microfractures have shown an exponential (Schubnel et al., 2007) or power law acceleration (Jones and Molnar, 1979; de Arcangelis et al., 2016) of activity when rupture is approached. Such irreversible dilation, if it can be monitored during the evolution of a given rock body towards rupture, could explain the increasing flux of chemical species before faulting (Hauksson, 1981; Tsunogai and Wakita, 1995; Toutain et al., 1997).

The main difference between our experiments and a mature fault is the existence of a pre-existing fault gouge and fault core. These have substantially lower strengths than the less-damaged wall rocks. The precursors may well be concentrated on the fault zone itself, particularly within the gouge. In addition, the precursory damage, and the signals associated with it, that do occur prior to large earthquakes may be quite different from the damage and the signals associated with the initial shear failure that occurred far in the past. Conversely, fault healing results in a cohesive re-strengthening (Weiss et al., 2016), and under these conditions, the shear failure of intact rock samples does have important similarities with natural faulting. The dilation and associated enhanced fluid conductivity probably occurs within the faults zone and would depend on pre-existing flow pathways, which are activated as rupture conditions are approached.

In the three modes of damage development (Figure 8), fractures are observed to form pervasively only for the Carrara marble (Figure 8b) and in the process zone during the development of fractures in the quartz monzonite (Figure 8a). However, in cases where compaction due to pore closure dominates (Figure 8c), it is unlikely that new fractures and paths for fluids would form and produce similar precursor signals. Therefore, the type and intensity of precursory signals should depend on the nature of the rock at depth. Because of the complexity of these precursors, it is important to incorporate microscale damage into fracture mechanics models, which provide a framework for linking macroscopic failure phenomena to microscopic deformation mechanisms (Pijaudier-Cabot and Bažant, 1987; Kachanov, 2013; Lyakhovsky et al., 1997; Lyakhovsky et al., 2015).

Microfracturing creates surface area in the rock, and the variation of the corresponding surface energy prior to failure can be estimated. Cumulating over all the voids detected by our tomographic measurements, we calculated the increase of surface area per unit volume prior to failure to be in the order of 500 m^2/m^3 for the monzonite and 2000 m^2/m^3 for the Carrara marble, given the voxel size resolution of 6.5 micrometer. To relate this with the global energy budget, we calculated the total mechanical work done by the rig on the sample during loading up to failure stress. It falls in the range 1-4 MJ/m^3 for these rocks, and of this 0.25-3 MJ/m^3 is irreversibly dissipated (see Table 2). Indeed, prior to a macroscopic failure, part of the elastic strain energy is dissipated through various mechanisms. The creation of new surfaces from fractures nucleation and propagation represents between 4% and 46% of this energy dissipation. Other dissipation mechanisms such as heat production, plastic strain at the microfractures tips, and microfractures below the resolution of the imaging are also possible. The large amount of

strain energy converted into fracture surface area is in favor of an elastic damage scenario in which the formation and propagation of microfractures are important precursors to failure.

The different ways in which damage evolves in different types of rock has implications for the evolution of the velocities of elastic waves in the vicinity of faults. The acoustic wave velocities were not measured directly during our experiments. However, the effect of damage on their amplitude variations can be estimated. Data of Figures 3 and 5 show that the change in porosity increased as the increasing differential stress drove the rock towards failure, reaching a value of $\Delta\phi = \pm 0.01$ for most samples at failure stress. Assuming a linear relationship between the compressive acoustic velocity V_p and porosity, V_p is equal to $(V_{p0} - \alpha\,\phi)$, where V_{p0} is the velocity at zero porosity, and α varies between 3-10 km/s (Mavko et al., 2009). Considering a typical value for V_{p0} of around 5 km/s and an initial porosity of $\phi_0=0.1$, with $\Delta V_p/V_p = -\alpha\Delta\phi / (V_{p0}-\alpha\phi_0)$, the variation of acoustic velocity related to damage is about ±0.6% at the onset of faulting. This variation represents a minimum because, due to the presence of microfractures oriented parallel to the main compressive stress, V_p anisotropy is expected to develop in the samples and larger acoustic waves velocities variations are expected (Schubnel and Guéguen, 2013). These variations of acoustic wave velocities are significant at the scale of the experiments. However, to be detected in nature they must occur in a rock volume large enough to be resolved by seismological inversion techniques.

Dynamic microtomography data reveal that rock density can either increase, remain constant, or decrease when shear faulting is approached. These results suggest that seismic, aseismic, and geochemical precursors to earthquakes or rock falls may vary significantly with the tectonic setting. Precursory signals to faulting, such as the amount and amplitude of microfractures, variations of acoustic wave velocity, and opening of fluid flow paths, strongly depend on the rock

present at depth, where a competition between microscopic dilation and compaction processes at the grain scale plays an important role in the path to macroscopic failure. Furthermore, in porous rocks, both compaction and dilation precursory events were observed simultaneously at different locations. Scaled to the field, this indicates that, depending on the location of a geophysical or geochemical sensor at the Earth's surface, the nature and amplitude of precursors to faulting could vary spatially.

References

Amitrano, D., Grasso, J. R., Senfaute, G., 2005. Seismic precursory patterns before a cliff collapse and critical point phenomena. Geophys. Res. Lett. 32, L08314.

Aydin, A., Johnson, A. M., 1978, Development of faults as zones of deformation bands and as slip surfaces in sandstones, Pure and Applied Geophysics 116(4-5), 931-942.

Bažant, Z. P., Kazemi,M. T., 1990. Determination of fracture energy, process zone length and brittleness number from size effect, with application to rock and concrete. Int. J. Fracture 44, 111-131.

Benson, P. M. Vinciguerra S., Meredith P. G., Young R. P., 2008. Laboratory simulation of volcano seismicity. Science 322, 249-252.

Bouchon, M., Karabulut, H., Aktar, M., Özalaybey, S., Schmittbuhl, J., Bouin M. P., 2011. Extended nucleation of the 1999 Mw 7.6 Izmit earthquake. Science 331, 877-880.

Bouchon, M., Durand, V., Marsan, D., Karabulut, H., Schmittbuhl, J., 2013. The long precursory phase of most large interplate earthquakes. Nature Geo. 6, 299-302.

Buades, A., Coll, B. & Morel, J. M., 2005. A non-local algorithm for image denoising, In Computer Vision and Pattern Recognition (IEEE Computer Society Conference, Vol. 2), pp. 60-65.

de Arcangelis, J., Godano, C., Grasso, J. R., Lippiello, E., 2016. Statistical physics approach to earthquake occurrence and forecasting. Physics Reports 628, 1-91.

Ellsworth, W. L. and Beroza, W. L., G., 1995. Seismic evidence for an earthquake nucleation phase. Science 268, 851-855.

Friedman, M., Handin, J., Alani, G. (1972) Fracture-surface energy of rocks. International Journal of Rock Mechanics and Mining Sciences & Geomechanics Abstracts 9, 757-764.

Guglielmi, Y., Cappa, F., Avouac, J. P., Henry, P., Elsworth, D., 2015. Seismicity triggered by fluid injection–induced aseismic slip. Science 348, 1224-1226.

Hall, S. A., 2013. Characterization of fluid flow in a shear band in porous rock using neutron radiography. Geophys. Res. Lett. 40, 2613-2618.

Hauksson, E., 1981. Radon content of groundwater as an earthquake precursor: evaluation of worldwide data and physical basis. J. Geophys. Res. Solid Earth 86, 9397-9410.

Jaumé, S. C., Lynn, R. S., 1999. Evolving towards a critical point: A review of accelerating seismic moment/energy release prior to large and great earthquakes. In Seismicity Patterns, their Statistical Significance and Physical Meaning (Birkhäuser Basel), pp. 279-305.

Jones, L. M., Molnar P., 1979. Some characteristics of foreshocks and their possible relationship to earthquake prediction and premonitory slip on faults. J. Geophys. Res. Solid Earth 84, 3596-3608.

352 Kachanov, L., 2013. Introduction to continuum damage mechanics (Springer, New York).

353 Kato, A., Terakawa, T., Yamanaka, Y., Maeda, Y., Horikawa, S., Matsuhiro, K., Okuda T., 2015.
354 Preparatory and precursory processes leading up to the 2014 phreatic eruption of Mount Ontake,
355 Japan. Earth, Planets and Space 67, 111.

356 Kato, A., Fukuda, J. I., Nakagawa, S., Obara, K., 2016. Foreshock migration preceding the 2016
357 Mw 7.0 Kumamoto earthquake, Japan. Geophys. Res. Lett. 43, 8945-8953.

358 Lenoir, N., Bornert, M., Desrues, J., Bésuelle, P., Viggiani, G., 2007. Volumetric digital image
359 correlation applied to X-ray microtomography images from triaxial compression tests on
360 argillaceous rock. Strain 43, 193-205.

361 Lockner, D., Byerlee, J. D., Kuksenko, V., Ponomarev, A., Sidorin, A., 1991. Quasi-static fault
362 growth and shear fracture energy in granite. Nature 350, 39-42.

363 Lyakhovsky, V., Ben-Zion, Y., Agnon, A., 1997. Distributed damage, faulting, and friction. J.
364 Geophys. Res. Solid Earth 102, 27635-27649.

365 Lyakhovsky, V., Zhu, W., Shalev, Y., 2015. Visco-poro-elastic damage model for brittle-ductile
366 failure of porous rocks. J. Geophys. Res. Solid Earth 120, 2179–2199.

367 Mair, K., Main, I., Elphick, S. 2000. Sequential growth of deformation bands in the laboratory,
368 Journal of Structural Geology 22(1), 25-42.

369 Mirone, A., Brun, E., Gouillart, E., Tafforeau, P., Kieffer, J., 2014. The PyHST2 hybrid
370 distributed code for high speed tomographic reconstruction with iterative reconstruction and a
371 priori knowledge capabilities. Nuclear Instruments and Methods in Physics Research Section B:
372 Beam Interactions with Materials and Atoms 324, 41-48.

373 Paterson, M. S., Wong, T. F., 2005. Experimental rock deformation-the brittle field, Springer,
374 New York.

375 Mavko, G., Mukerji, T., Dvorkin, J., 2009. The rock physics handbook: Tools for seismic
376 analysis of porous media (Cambridge University Press, Boston).

377 Pijaudier-Cabot, G., Bažant, Z. P., 1987. Nonlocal damage theory. J. Eng. Mech. 113, 1512-1533.

378 Renard, F., Cordonnier, B., Dysthe, D. K., Boller, E., Tafforeau, P., Rack A., 2016. A
379 deformation rig for synchrotron microtomography studies of geomaterials under conditions down
380 to 10 km depth in the Earth. J. Synch. Rad. 23, 1030-1034.

381 Schubnel, A., Thompson, B. D., Fortin, J., Guéguen, Y., Young, R. P., 2007. Fluid-induced
382 rupture experiment on Fontainebleau sandstone: Premonitory activity, rupture propagation, and
383 aftershocks. Geophys. Res. Lett. 34, L19307.

384 Schubnel, A., Guéguen, Y., 2013. Dispersion and anisotropy of elastic waves in cracked rocks. J.
385 Geophys. Res., 108, 2101.

386 Sugan, M., Kato, A., Miyake, H., Nakagawa, S., Vuan, A., 2014. The preparatory phase of the
387 2009 Mw 6.3 L'Aquila earthquake by improving the detection capability of low-magnitude
388 foreshocks. Geophys. Res. Lett. 41, 6137-6144.

389 Toutain, J. P., Munoz, M., Poitrasson, F., Lienard, A. C., 1997. Springwater chloride ion anomaly
390 prior to a ML= 5.2 Pyrenean earthquake. Earth Planet. Sci. Lett. 149, 113-119.

391 Tsunogai, U., Wakita, H., 1995. Precursory chemical changes in ground water: Kobe earthquake,
392 Japan. Science 269, 61-63.

Wakita, H., 1996. Geochemical challenge to earthquake prediction. Proc. Natl. Acad. Sci. U.S.A. 93, 3781-3786.

Weiss, J., Pellissier, V., Marsan, D., Arnaud, L., Renard, F., 2016. Cohesion versus friction in controlling the long-term strength of a self-healing experimental fault. J. Geophys. Res. Solid Earth 121, 8523–8547.

Zang, A., Wagner, F. C., Stanchits, S., Janssen, C., & Dresen, G. 2000. Fracture process zone in granite. J. Geophys. Res. Solid Earth, 105, 23651-23661.

Zhu, W., Baud, P. & Wong, T. F., 2010. Micromechanics of cataclastic pore collapse in limestone. J. Geophys. Res. Solid Earth 115, B04405.

Zhu, W., Fusseis, F., Lisabeth, H., Xing, T., Xiao, X., De Andrade, V., Karato, S., 2016. Experimental evidence of reaction-induced fracturing during olivine carbonation. Geophys. Res. Lett. 18, 9535-9543.

Acknowledgements. The deformation apparatus was built by Sanchez Technology. Elodie Boller, Paul Tafforeau, and Alexander Rack provided advices on the design of the tomography setup; Paul Meakin provided suggestions on an early version of this article, and Catherine Noiriel, Florian Fusseis, Jesús Rodriguez-Sánchez, and Xiaojiao Zheng helped with the tomography data acquisitions. This study received funding from the Norwegian Research Council (project HADES, grant 250661), the European Union (H2020 ERC Advanced Grant DIME), and beamtime was allocated at the European Synchrotron Radiation Facility (Long Term Proposal ES-295). Partial support for WZ was provided by the US National Science foundation through

414 grant NSF-EAR1056317. The authors thank C. Scholz and an anonymous reviewer for their
415 constructive suggestions.

416

417 **Author contributions**. F.R. conceived the research, acquired and analyzed data, and wrote the
418 paper. W.Z. and J.W. contributed to the discussion and manuscript preparation. B.C., M.K., and
419 N.K acquired and analyzed data.

420

421 **Supplementary Information**

422 Figs. S1 to S3
423 Videos S4 to S6

Tables and figures

Sample #	Ø (mm)	P_c (MPa)	Y (MPa)	σ_f (MPa)	E (GPa)	ϕ_i	Nb. 3D scans
Quartz monzonite 3	4	20	261	273	22.6	0,13%	72
Fontainebleau sandstone 2	5	10	150	168	15.2	11%	47
Carrara marble 1	5	20	77	97	11.4	0,44%	45
Carrara marble 2	5	25	128	148	14.2	0,15%	97
Anstrude limestone 2	5	20	68	72	8.4	16%	41
Anstrude limestone 3	5	5	34	38	5.6	16%	26
Anstrude limestone 4	5	20	54	65	4.5	16%	55
Anstrude limestone 5	5	5	44	51	3.6	16%	27
Adamswiller sandstone 1	5	30	111	133	12.9	13%	57
Bentheim sandstone 1	5	5	63	76	16.5	19%	78

Table 1: Rock sample characteristics and experimental conditions. Ø: sample diameter; P_c: confining pressure; Y: yield stress, σ_f: differential stress at faulting, E: Young's modulus, ϕ_i: initial porosity. The number of 3D tomography volumes acquired during each experiment is given.

Sample #	E	ε_0	σ_f	ε_f	SA	γ_0
	GPa	-	MPa	-	m^2/m^3	J/m^2
Carrara marble 1	1,1E+01	2,2E-03	9,7E+01	1,9E-02	1,8E+03	5,0E+01
Carrara marble 2	1,4E+01	1,4E-02	1,5E+02	4,3E-02	2,6E+03	5,0E+01
Quartz monzonite 3	2,3E+01	2,0E-03	2,2E+02	1,1E-02	5,2E+02	5,0E+01

Sample #	Ω_1	Ω_2 , $\varepsilon=0$	Ω_2 , $\varepsilon=\varepsilon_0$	Ω_3	$\Omega_1 - \Omega_2$, $\varepsilon=0$	Ω_1 - Ω_3	$\gamma = \gamma_0$ x SA	$\gamma/(\Omega_1 - \Omega_2)$	$\gamma/(\Omega_1 - \Omega_3)$
	J/m^3	J/m^3	J/m^3	J/m^3	J/m^3	J/m^3	J/m^3		
Carrara marble 1	1,1E+06	9,3E+05	8,2E+05	4,4E+05	1,9E+05	6,8E+05	8,9E+04	46%	13%
Carrara marble 2	4,1E+06	3,6E+06	2,4E+06	9,8E+05	4,6E+05	3,1E+06	1,3E+05	28%	4%
Quartz monzonite 3	1,3E+06	1,2E+06	1,0E+06	1,1E+06	8,7E+04	2,5E+05	2,6E+04	30%	10%

Table 2: Top: Material parameters (E: Young's modulus, σ_f: axial stress at failure, SA: surface area of damage at failure, γ_0: surface energy of the rock; ε_0: strain when removing the initial crack closure; ε_f: strain at failure). Bottom: Estimation of the energy budget in the experiments for three samples (Carrara marble, quart monzonite). The energy densities Ω_1, Ω_2, Ω_3 are defined in the Figure 7 and estimations of the ratios between damage due to surface energy and total strain energy due to the loading of the sample are given.

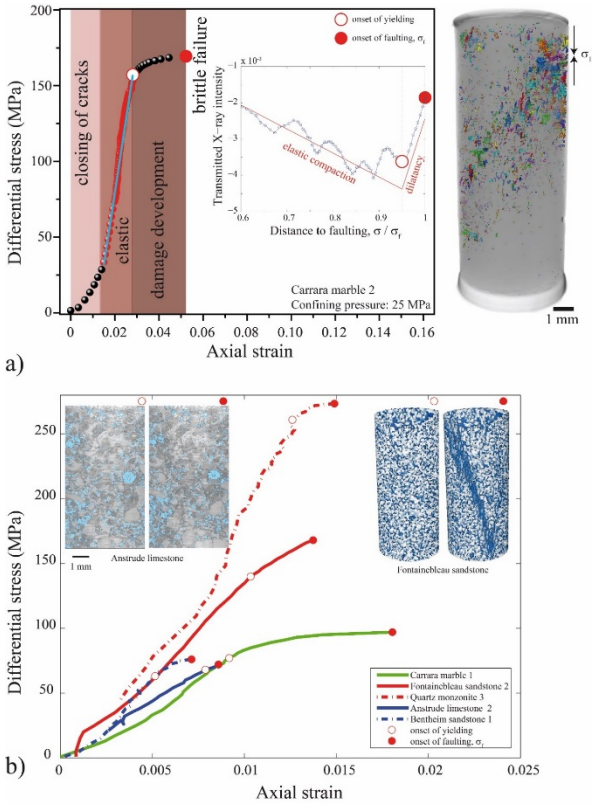

Figure 1: Stress-strain relationships and damage development prior to faulting. a) Stress-strain curve for a Carrara marble sample deformed at 25 MPa confining pressure. For each differential stress increment a 3D volume was imaged. At low stress, some microfractures initially present in the sample closed. Then, as the axial stress was increased, the sample deformed elastically with a more-or-less linear relationship between strain and stress. At the yield point (empty circle), irreversible deformation occurred, and the curve became non-linear, until faulting occurred (solid circle). The inset shows the corresponding X-ray absorption signal, with an increase of intensity as damage (i.e. porosity) developed towards faulting. On the right hand side, the sample is viewed in 3D with all individual damage events at the onset of faulting. b) Stress-strain curves of representative rocks deformed until faulting. Insets shows 3D views of a Fontainebleau sandstone and 2D views in the middle of an Anstrude limestone at the onset of yielding and onset of faulting, respectively. Void spaces are shown in blue.

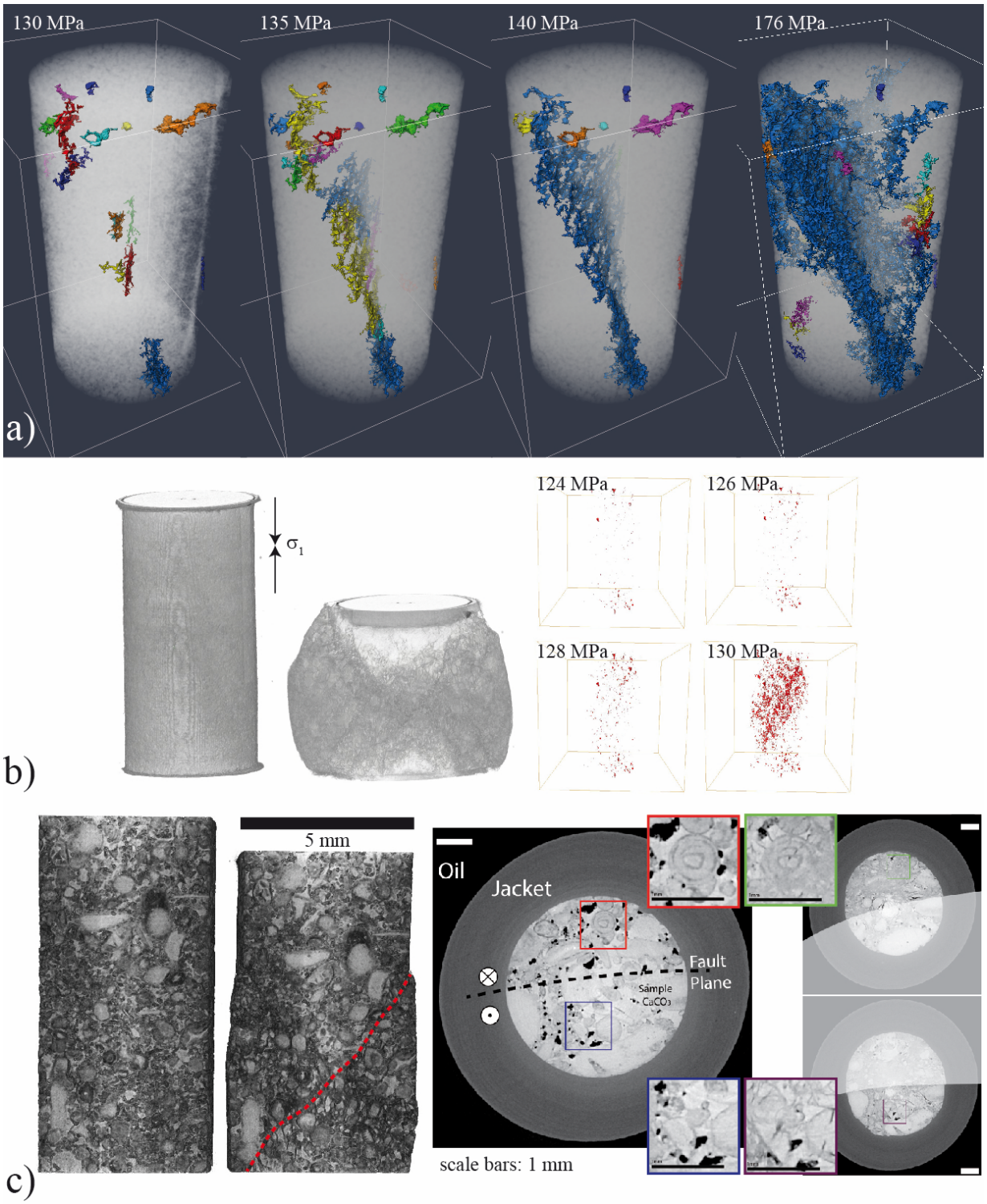

Figure 2: Development of damage and faulting in various rocks visualized by in-situ X-ray microtomography. a) Development of a shear fracture into Fontainebleau sandstone with

differential stress increasing by steps of 1 MPa from 130 MPa (left) to 176 MPa (right). The confining pressure was 10 MPa. The rock is shown in a translucent white color and the largest connected fractures are shown in various colors. b) Carrara marble at a confining pressure of 20 MPa before (left) and after (right) faulting. Dilatant behavior due to the pervasive nucleation and growth of microfractures (in red) initiated at the onset of yielding. This damage concentrated onto a band that evolved into a shear fault. c) Deformation of an Anstrude limestone at 20 MPa confining pressure until faulting. 3D view rendering before (left) and after (right) faulting, with the shear fault indicated by the dashed line. 2D slice images in the middle of the sample before (left) and after (right) faulting. Damage was mainly due to the collapse of pores prior to faulting.

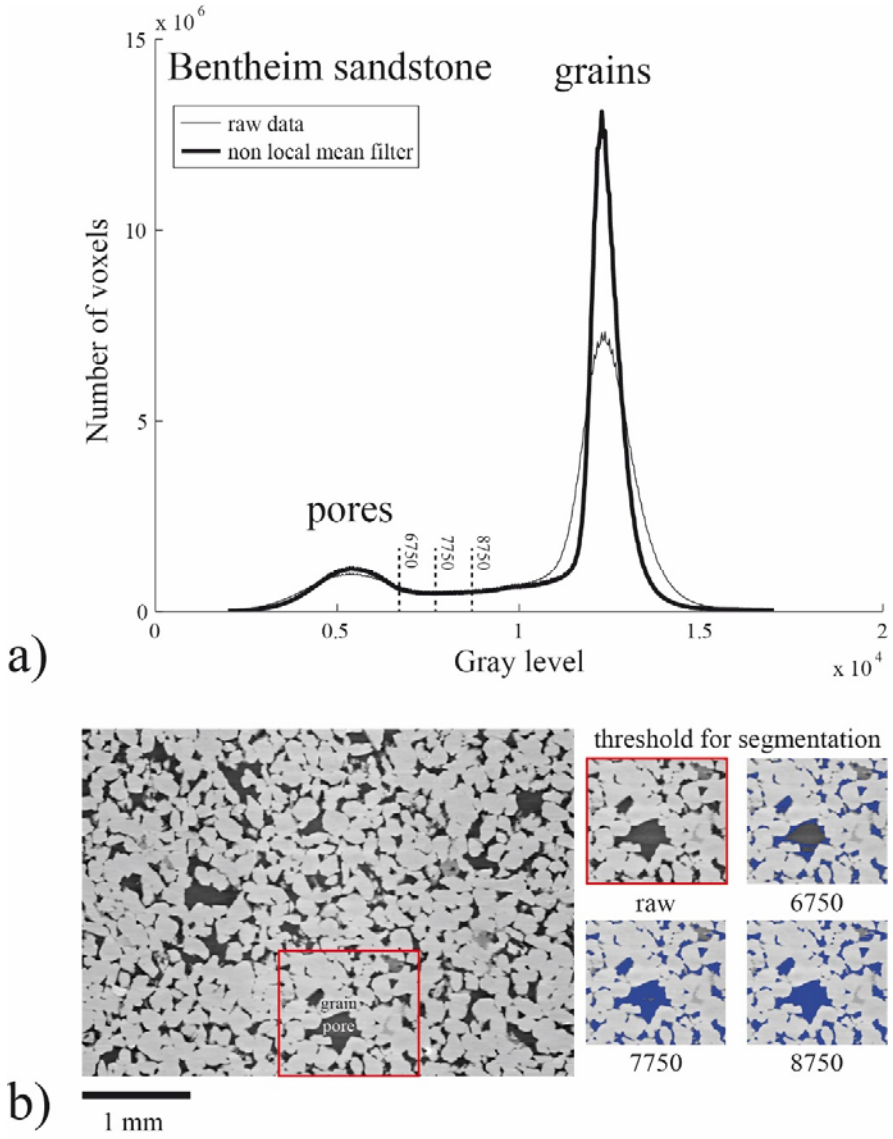

463

464 **Figure 3**: a) Histogram of X-ray gray levels in a Bentheim sandstone sample with raw (thin line)
465 and denoised (thick line) data. The two peaks correspond to pores and grains, respectively. The
466 three thresholds used to perform the segmentation for the data of Figure 4 are indicated. The
467 minimum of the histogram corresponds to the gray level value of 7750. b) 2D slice of the
468 Bentheim sandstone and effect of three different gray level thresholds on the segmentation of the
469 pore space.

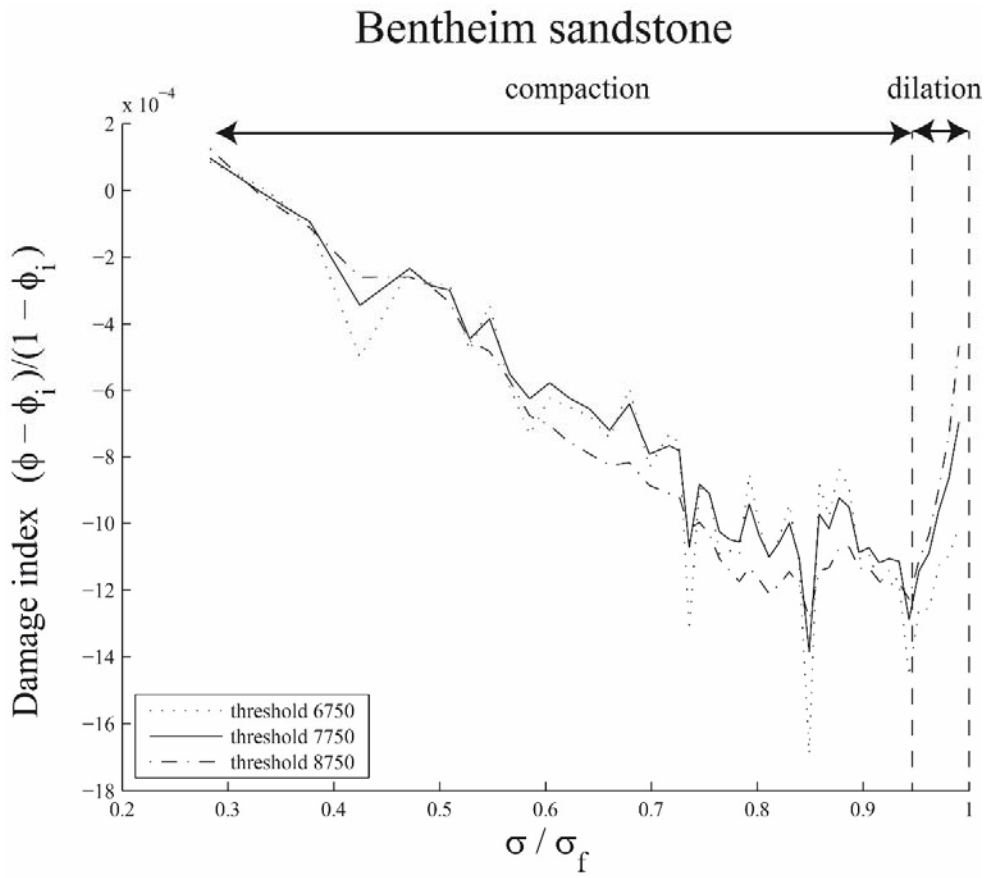

Figure 4: Evolution of the damage index towards faulting for a Bentheim sandstone sample. The deformation is characterized by compaction as the differential stress is increased, and then some dilation when approaching faulting. The three curves correspond to the three thresholds used for segmenting the pore space in Figure 3 and show the same trend, independently on the choice of the threshold. The minimum of the histogram in the Figure 3a corresponds to the gray level value 7750.

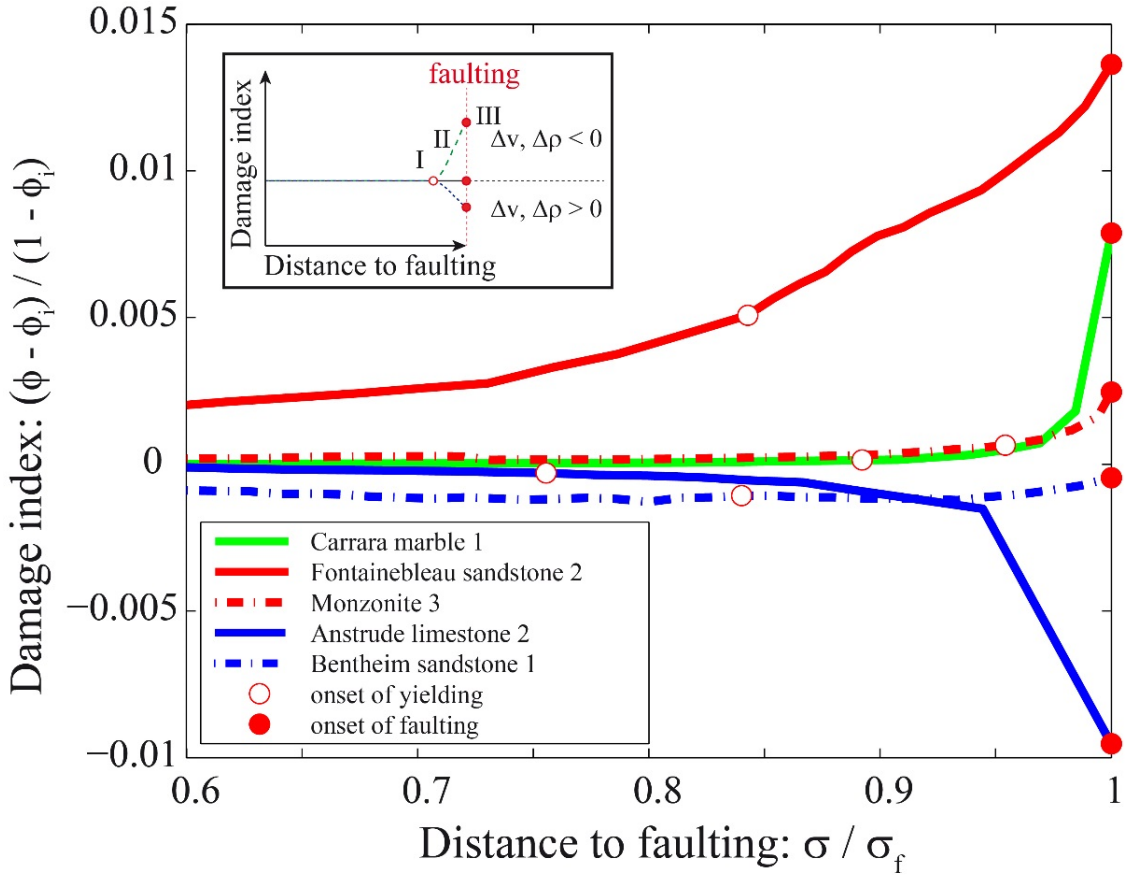

477

478 **Figure 5**: Evolution of damage index as the stress is increased towards the faulting stress σ_f. The
479 damage index can increase, decrease, or remain constant, depending on rock type. Inset: The
480 damage index is the total void volume fraction ϕ relative to the initial value ϕ_0 in the rock. When
481 the damage index increases, the density ρ and seismic velocity v of the material decrease, and vice-
482 versa. The sketch shows the onset of yielding (I), strain localization (II), and faulting (III).

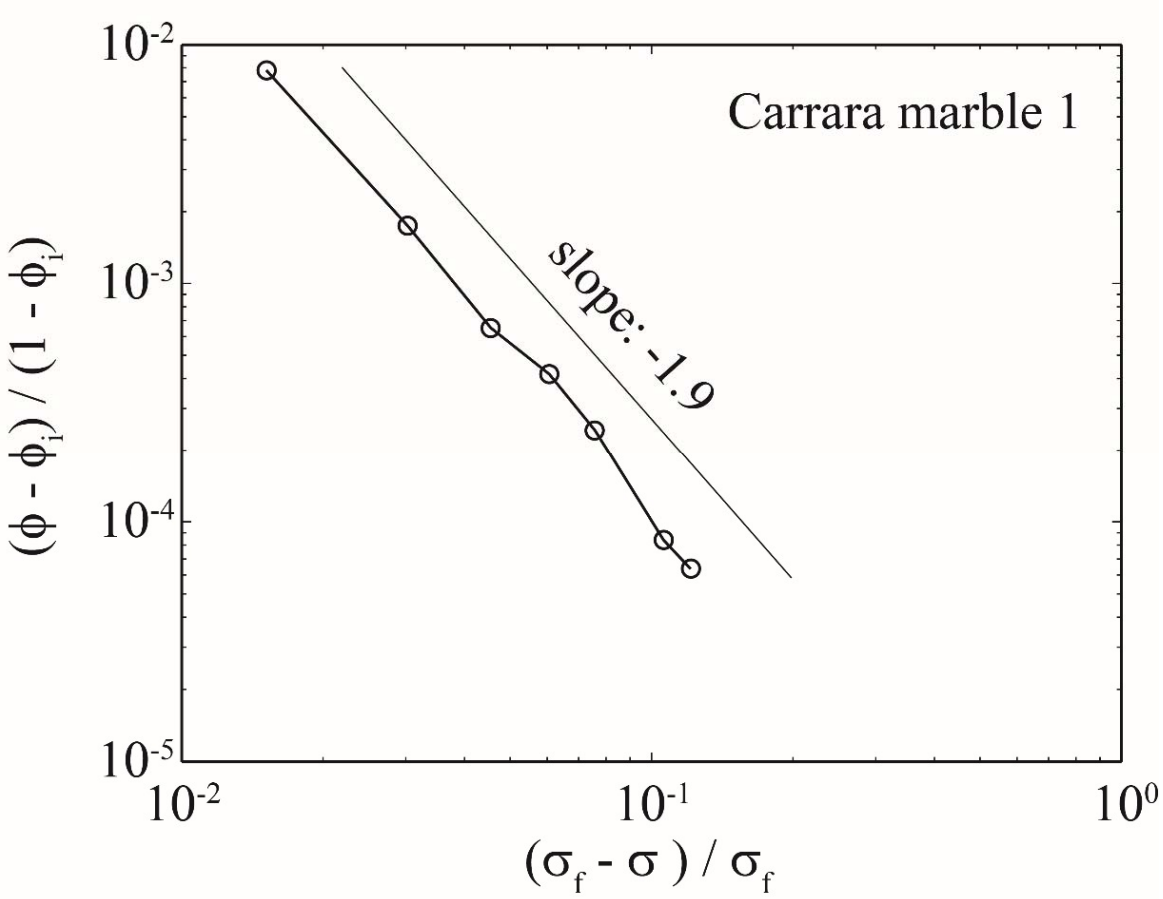

Figure 6: Evolution of the damage index for the Carrara marble towards failure displayed on a log – log scale. The straight line corresponds to a power law $\frac{\phi-\phi_i}{1-\phi_i} \sim \left(\frac{\sigma_f-\sigma}{\sigma_f}\right)^{-\nu}$ with an exponent of 1.9. Failure occurs when the normalized stress $(\sigma_f - \sigma)/\sigma_f$ reaches zero. Each circle corresponds to a 3D volume acquired before failure.

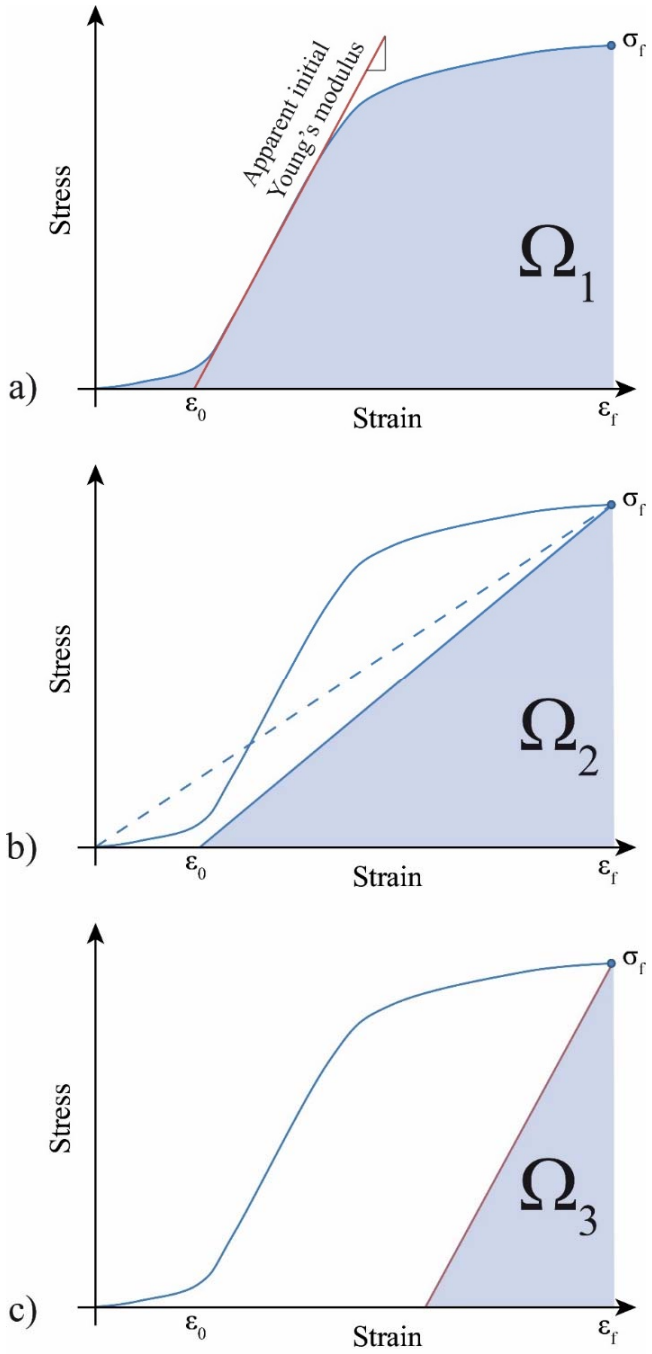

488

489 **Figure 7**. Strain energy during the loading phase of each sample. The surface Ω_1 corresponds to
490 the mechanical work stored in the sample during loading and is the integral of the stress-strain
491 curve. The surfaces Ω_2 and Ω_3 correspond to two extreme cases of the recovered elastic strain
492 energy release upon unloading for a purely elastic damaged or a plastic solid, respectively.

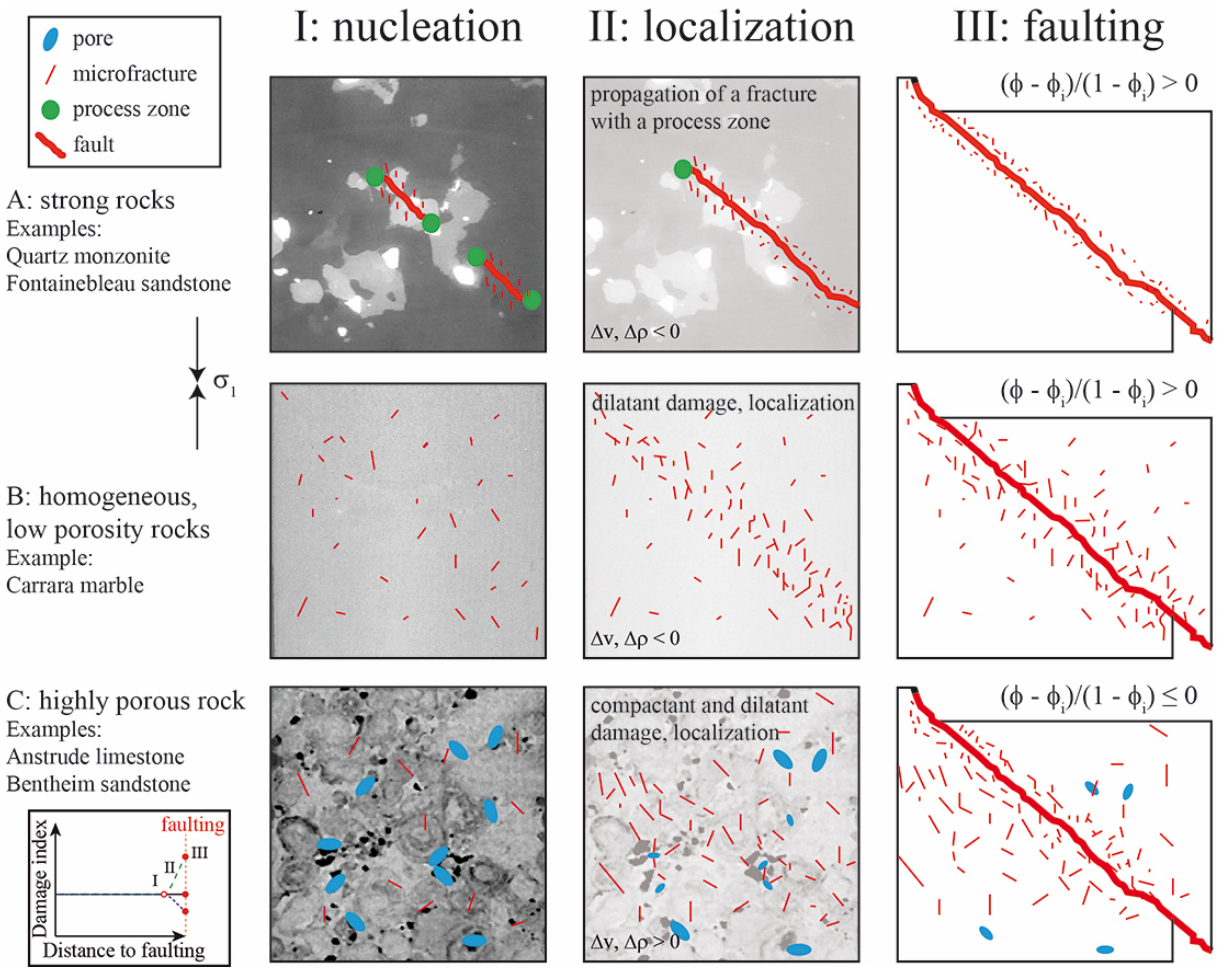

Figure 8: Variety of damage dynamics as stress is increased towards faulting. Phases I, II, and III correspond to the nucleation of damage at the onset of yielding, localization (during which rock density ρ and acoustic waves velocity v vary), and faulting, respectively. A) Growth of several fractures along a localized plane. At the tip of each fracture some damage develop in the form of vertical cracks. B) Pervasive damage (microfractures, shear bands) localizing onto a single shear plane. C) Interaction between dilatant damage (microfractures, in red) and compaction damage (collapse of pore, in blue) and strain localization along a shear fault. Typical microstructures are shown in the background (A: Quartz monzonite, B: Carrara marble, C: Anstrude limestone). Inset: same as in Figure 5.

Supplementary Information

Caption: Sketch of the experimental set-up (Fig. S1). Differential stress versus strain (Fig. S2) and damage index versus stress at failure (Fig. S3) for all samples analyzed in the present study. Three videos are provided that show the 3D evolution of rock samples towards failure (Videos S4 to S6).

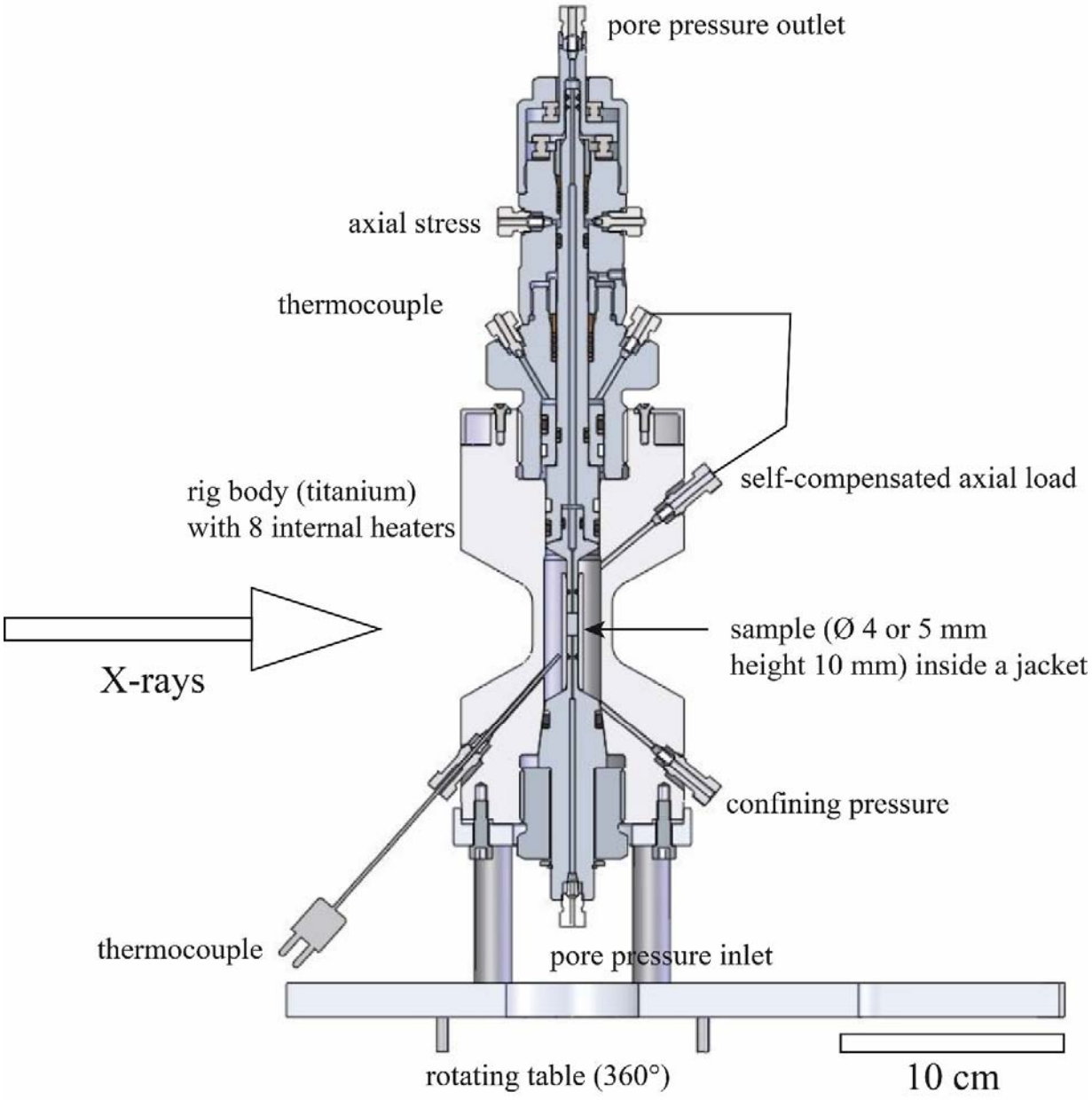

Figure S1: Sketch of the HADES triaxial deformation rig (Renard et al., 2016). The sample is surrounded by a jacket made of Viton and confined with oil. The axial load is imposed by a stainless steel piston. The axial load, confining pressure, inlet pore fluid pressure, and outlet pore fluid pressure are controlled independently by four pumps. The body of the rig contains eight internal heaters for temperature control. The rig is installed on the X-ray microtomography stage at beamline ID19 at the European Synchrotron Radiation Facility in Grenoble, France.

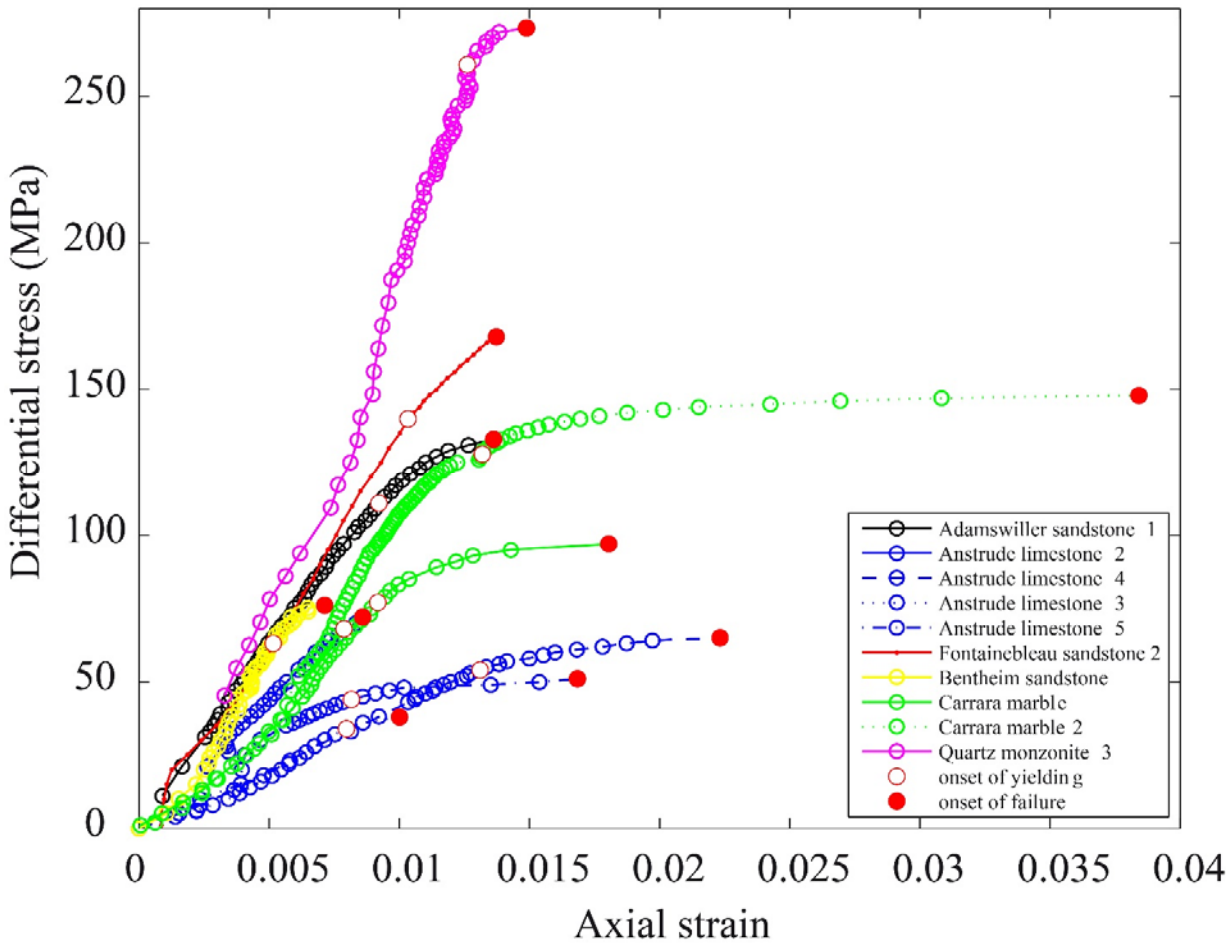

515

516 **Figure S2**: Stress-strain relationships for all samples deformed in the present study (see figure

517 1b). Each circle corresponds to data for one three-dimensional image at a given stress step.

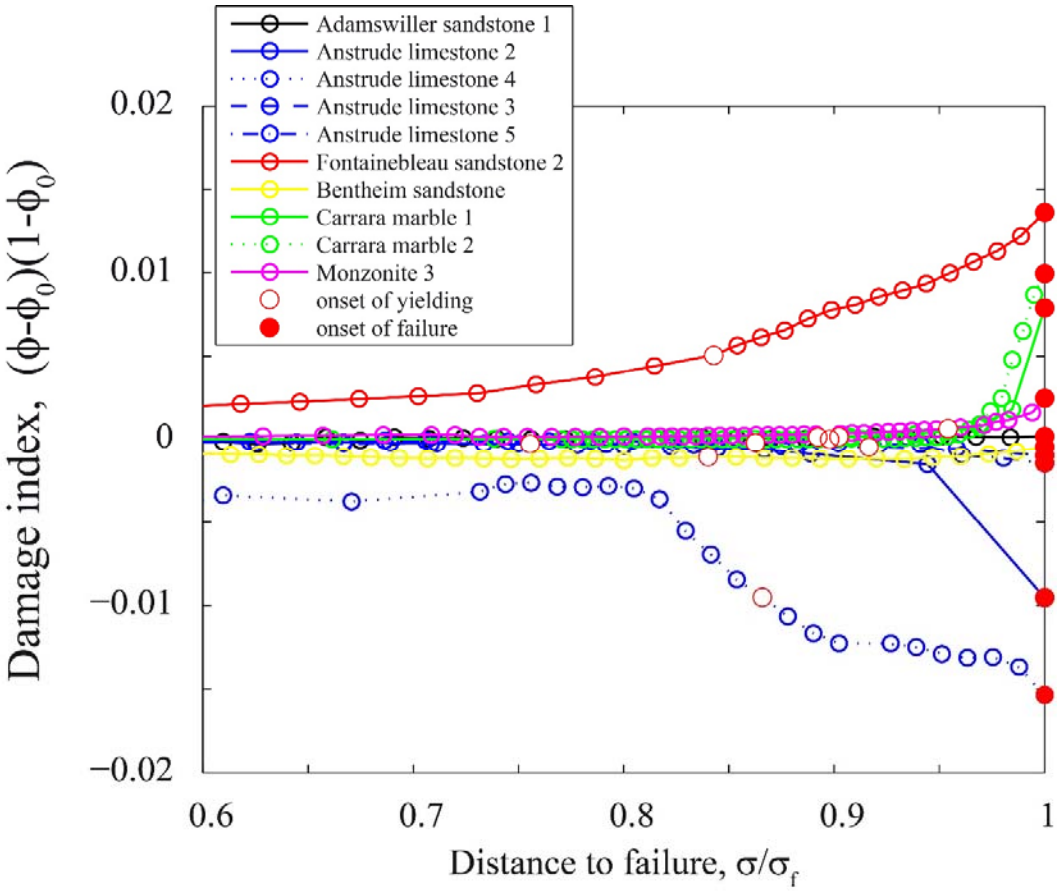

518

519 **Figure S3**: Evolution of the damage index towards faulting for all samples deformed in the
520 present study (see Figure 5). Each circle corresponds to data for one three-dimensional image at a
521 given stress step.

Video S4: Growth of a shear fault in a quartz monzonite sample (diameter 4 mm). The pore and damage spaces are shown in blue, and the rock in white and gray. The 3D rendering in false color shows progressive damage until failure. The movie shows the entire experiment until failure. The stress-strain curve is added.

Video S5: Nucleation and growth of damage (microfracturing) and faulting in a Carrara marble sample (diameter 5 mm). The 3D rendering in false color shows progressive damage until failure. The movie shows the entire experiment until failure.

Video S6: Damage by pore collapse and microfracturing and faulting in an Anstrude limestone (sample diameter 5 mm). The 3D rendering in false color shows progressive damage until failure. The movie shows the entire experiment until failure.